Composite Structures 135 (2016) 339–352

Contents lists available at ScienceDirect

Composite Structures

journal homepage: www.elsevier.com/locate/compstruct

A numerical study of auxetic composite panels under blast loadings

Gabriele Imbalzano [a], Phuong Tran [b], Tuan D. Ngo [b,*], Peter V.S. Lee [a]

[a] Department of Mechanical Engineering, The University of Melbourne, VIC, Australia
[b] Department of Infrastructure Engineering, The University of Melbourne, VIC, Australia

ARTICLE INFO

Article history:
Available online 30 September 2015

Keywords:
Auxetic composite
Blast performance
Composite sandwich
Finite-element simulation
Negative Poisson's ratio

ABSTRACT

Sandwich panels composed of auxetic cellular cores and metal facets are presented for blast resistance applications. The performance of this hybrid composite structure under impulsive loading is numerically studied, taking into account the rate-dependent effects. The Johnson–Cook law is used to model the behaviours of composite materials at high strain rates. Parametric analyses are performed to evaluate the performances of different designs of composite panels and compared with equivalent monolithic panels of identical areal masses in terms of deformations and dissipated plastic energy of the metal facets and auxetic crushable cores. Various design parameters are considered, including the auxetic unit cell effective Poisson's ratio, material properties, thickness of facet, and diameter of the unit cell truss member. To reduce the computational time, a quarter of the panel is modelled with shell elements for the facets and beam elements for the core. In blast events, auxetic composite panels are found to effectively absorb double the amount of impulsive energy via plastic deformation, and reduce up to 70% of the back facet's maximum velocity when compared with monolithic ones. The maximum back facet displacement is also noticeably reduced by up to 30% due to the densification and plastic deformation of the auxetic cores.

1. Introduction

The design of new smart and lightweight materials and structures for energy-absorbing purposes is complex, requiring the structure to be able to withstand and mitigate blast loadings whilst still being light in weight [1–5]. Auxetic structures, which exhibit negative Poisson's ratio (NPR) effect, could offer a potential alternative solution to address these concurrent objectives. Auxetic materials are normally characterised by counterintuitive behaviour as they contract laterally (densification) under compression and expand when stretched [6]. With such mechanical behaviours, they are shown to provide some enhancements in physical properties, such as higher fracture toughness, indentation resistance, shear modulus and vibration absorption, as well as lower fatigue crack propagation [7–10]. Lakes and Elms [11] performed indentation tests on auxetic and conventional copper foams. They demonstrated that auxetic foams have greater yield strength and lower stiffness than conventional ones, and their energy absorption for impact is greater. Scarpa et al. [12,13] compared auxetic and conventional foams to assess their static and dynamic characteristics, and the strength values were around one order of magnitude higher for auxetic foams under constant strain rate (between 8 and 12 s^{-1}) compression. Other studies on auxetic fibre reinforced composites [14] showed an enhancement of mechanical properties with static indentation and low velocity impacts, as well as an increase in resistance to fibre pull-out. Moreover, the damage results are much more localised, enabling smaller reparations. Studies on graded conventional–auxetic sandwich structures [15] have demonstrated the potential use of auxetic and graded conventional–auxetic structures under flatwise compression and edgewise loading. It was shown that if the auxetic structure faces perpendicularly to the loading, the maximum displacement is 2.8 mm, while that of conventional structure is 7 mm. The damage localisation of the auxetic structures was one key force-resistance factors together with the cell size and orientation.

Since the early trial by Lakes in 1987 to manufacture an auxetic foam [6], significant efforts have been devoted to the development of NPR materials from polymers, metals, ceramics, or other inert materials as well as structures. Various types of auxetic cellular structures are also designed and analysed experimentally and analytically, such as the 2D truss systems with periodic chiral unit cells [16], NPR re-entrant structures [17,18], or rotating rigid/semi-rigid auxetic unit cells [19]. Three-dimensional auxetic structures have also been developed as an auxetic frame [20], multi-pod lattice [21], and quasi-bow-tie elements [22]. There are still, however, many challenges for the fabrication of 3D structures due to technological limitations [23].

* Corresponding author.
E-mail address: dtngo@unimelb.edu.au (T.D. Ngo).

http://dx.doi.org/10.1016/j.compstruct.2015.09.038
0263-8223/

Considerable efforts have also been devoted to the design and manufacture of stiff and lightweight composite structures due to the fast-growing defence and civilian industry interests [24–30]. There are various applications that require high-performance materials to withstand high strain rate loadings; for example, ship hulls subjected to underwater explosions [4,31] or automobile parts designed for crash absorption. The most effective approach is to use sandwich structures, which combines two solid facets and a foam core for blast mitigation. It has been demonstrated that a crushable core, which can dissipate a substantial amount of energy, could weaken the transmitted shockwave to the back-side facets and therefore protect them from critical failure. There are a number of studies on metallic sandwich architectures that show that they outperform monolithic structures of equal areal mass [5,32–34,1].

Although auxetic materials have been extensively investigated for their mechanical properties, mostly under static or quasi-static loading conditions, understanding on the behaviours of NPR structures subjected to extreme loadings is very limited. Ma et al. [35] developed a sandwich panel with a functional-graded auxetic core for blast resistance. Schenk et al. [36] investigated the performance of a stacked, folded auxetic core in a sandwich beam structure under static compression and impulsive loadings. For blast mitigation, it is important to incorporate the auxetic core into sandwich panels, where the external facets could be used to prevent severe localised damage on the energy absorbing layers. Although additive manufacturing technology could be used to fabricate an auxetic unit cell for small- to medium-scales with different choices of shapes, there are still considerable challenges associated with cost and fabrication. As a result, the development of predictive numerical models for auxetic structures is necessary to provide the initial design concepts and insights into the dynamic responses of the auxetic composite panel (ACP) under extreme loadings. However, detailed modelling for NPR unit cells in large-scale ACP panels could be extremely computationally intensive, which is not addressed in the literature.

In this paper, we will develop an effective numerical model to simulate auxetic composite sandwich panels subjected to blast loadings. A selected 3D auxetic unit cell, which is a natural extension from a well-known 2D re-entrant NPR structure [7] and a 3D re-entrant elongated dodecahedron [37] to obtain the auxetic behaviour also in the transverse planes. This 3D model will be simulated using beam elements and assembled into three-layers ACP cores sandwiched between two metallic facets. Detailed numerical and material model developments will be presented in Section 2, followed by the results and discussion. The last section will present various parametric studies on the influence of slenderness of auxetic structures, effective Poisson's ratio, thickness of the metal facet, and the choice of material on blast resistance performance.

2. Numerical model for auxetic composite structure

2.1. Auxetic unit cell model

The auxetic unit cell (AU), the sandwich composite structure investigated in this work, is presented in Fig. 1. It has a re-entrant shape and has been chosen to exhibit a negative Poisson's ratio (NPR) effect. The structure is relatively simple for design and fabrication. Its 3D geometry is a natural extension from a popular 2D re-entrant AU, providing the biaxial NPR responses from all loading directions compared to the uniaxial behaviour of the 2D AU. Furthermore, the truss structure provides a higher strength-to-weight ratio when compared with a honeycomb structure and could be easily tailored for different applications [38,39]. In another aspect, it can also preserve the auxetic behaviour for large strains, which is important for structures under extreme loading threats. Finally, its simple structure could be tailored and realised quickly to adapt to different loadings by adjusting key geometrical factors and using additive manufacturing fabrication.

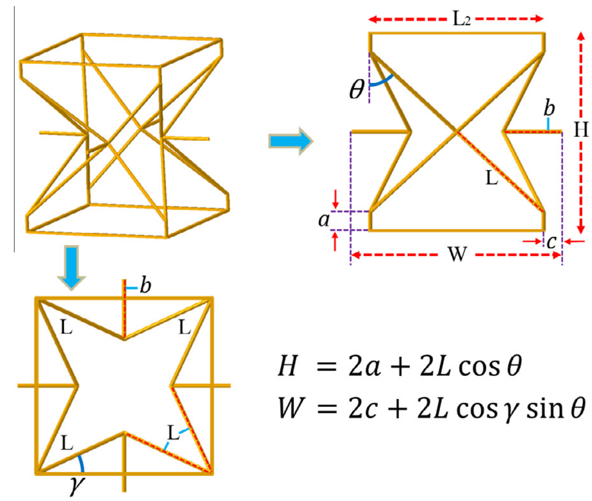

Fig. 1. Schematic design of 3D auxetic unit cell.

The AU configuration is defined by two angles, θ (from 10° to 80°) and γ (from 5° to 40°); and the length, L, of the diagonal strut member. The baseline structure is presented in Fig. 1 with $\theta = 50°$, $\gamma = 20°$ and $L = 6.7$ mm. The set ranges for angle parameters are to prevent contact between the struts and to enable effective auxetic behaviour. The height of the vertical connection strut is defined as $a = 1$ mm; while the horizontal linking struts are calculated as $b = L\cos(\gamma)\sin(\theta)(1-\tan(\gamma)) + c$, with $c = 1$ mm. All the diagonal, connecting and linking struts are assumed to have a circular cross-section with a radius of r; and the remaining eight struts forming the top and bottom bases of the unit cell have square cross-sections of width d. For the baseline case given in Fig. 1, $r = 0.2$ mm and $d = 0.4$ mm. The dimensions have been chosen to be manufacturable by an advanced selective laser sintering (SLS) additive manufacturing technique with resolution reaching 40 μm. The base of the unit cell has a square shape, with the width calculated as $L_2 = 2L\cos(\gamma)\sin(\theta)$. The total height of the structure is $H = 2a + 2L\cos(\theta)$ and the total width is $W = 2c + L_2$. Therefore, the relative density, ρ^*, which is the ratio of the material volume of the AU structure versus the total volume, is calculated as:

$$\rho^* = \frac{1}{2}\frac{(4L + L\sin(\gamma)\sin(\theta) + c + 2a)\cdot\pi r^2 + 4L\cos(\gamma)\sin(\theta)\cdot d^2}{[L\cos(\gamma)\sin(\theta) + c]^2\cdot(a + L\cos(\theta))}. \quad (1)$$

2.2. Effective Poisson's ratio of auxetic unit cell

The effective Poisson's ratio (EPR) v_{zx} of the AU is defined as the ratio between the transverse engineering strain associated with the horizontal displacement, and the axial engineering strain calculated from the relative vertical displacement. The procedure of calculating EPR is illustrated in Fig. 2. The model is constructed in ABAQUS and uniform static loading is applied on the top base of the AU, while the bottom one is simply supported in the vertical direction. Displacements, strains and EPR are then calculated numerically.

The effects of the θ and γ angles are also presented in Fig. 2 for fixed values of all the struts similar to the baseline case. The two axes are constrained from 10° to 80° for θ, and from 5° to 40° for γ. As can be seen from Fig. 2, the effective Poisson's ratio v_{zx} could vary from 0 to −21. In particular, it was noticed that the smaller

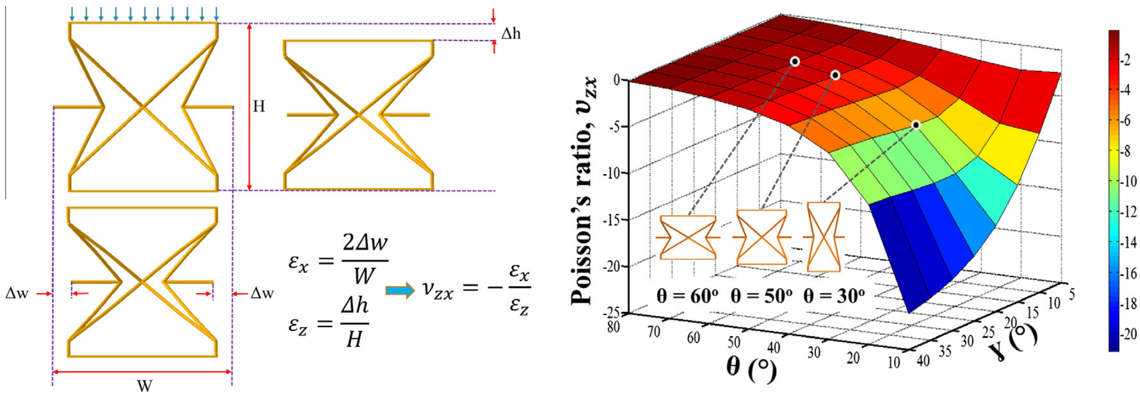

Fig. 2. Calculation procedure for effective Poisson's ratio $\boldsymbol{\nu_{zx}}$ (EPR) of the auxetic unit cell (left) and dependence of EPR on geometrical parameters of the unit cell (right).

the value of θ, the higher the absolute value of the EPR. For the remainder of the studies, two parameters are kept constant, including $\gamma = 20°$, which is a reasonable value to avoid manufacturing issues, and $L = 6.7$ mm as in the baseline case. AU structures associated with three values of θ as 30°, 50° and 60° are analysed for EPRs, which give the corresponding value of $\boldsymbol{\nu_{zx}} = -6.15$, -1.94 and -1.03. The unit cell associated with $\theta = 50°$ coincides with the configuration of the baseline model. Comparing the shapes of the three AUs suggests that the smaller value of θ gives a taller and more slender unit cell.

As the proposed unit cell structure is anisotropic, it is also important to evaluate the Poisson's ratio $\boldsymbol{\nu_{xz}}$. Similar single unit cell model developed for the previous analysis has been employed. A static load is applied laterally to compress the linking beams of the unit cell, from which displacements, strains and Poisson's ratio $\boldsymbol{\nu_{xz}}$ could be calculated numerically as shown in Fig. 3.

AU structures with the values of θ as 30°, 50° and 60° are analysed, and the corresponding values of $\nu_{xz} = -0.08$, -0.31 and -0.58 are obtained. The Poisson's ratio in the perpendicular direction is still negative, but smaller than the corresponding values of ν_{xz}. As the auxetic structure is designed to withstand extreme compressive loadings, the choice of AU geometrical configuration is important to avoid early local buckling effects of slender structures and to maximise the energy absorption capacity.

2.3. Auxetic unit cell finite element model and convergence study

Two different finite element (FE) models for the auxetic unit cell are implemented and compared here including a full 3D model, in which all AU struts are discretised by 19,830 tetrahedral modified second-order solid elements (C3D10M). The second AU is simply modelled by three-node second-order Timoshenko beam elements (B32), which takes into account transverse shear stiffness of the beam. The total number of elements is between 48 and 160 for different mesh densities. The number of elements used in each approach is vastly different, which could significantly affect the computational time. These models are assumed to have no local imperfections, which could be introduced and investigated in later sections for their influences on auxetic behaviours. Such localised imperfections could be expected due to possible surface roughness and porosity of the 3D additive manufactured unit cells.

Fig. 4 presents different approaches in modelling the AU including a full 3D tetrahedral solid mesh (Fig. 4a) and a beam-based discretisation (Fig. 4b and c). The solid element model has a very refined mesh (approximately 0.1 mm) and the elements are chosen to prevent volumetric locking and the hourglass effect [40]. With such FE mesh discretisation, the solid AU model contains up to 19,830 elements. In the second approach, the AU structure is reproduced with B32 beam elements for all struts (Fig. 4b and c). The diagonal and vertical struts are modelled to have a circular cross-section with constant radius. The definition of contacts between beams, which has been recently introduced in ABAQUS 6.13, is employed and defined to capture the densification behaviour of the AU under compression more accurately. The vertical struts (in green colour and marked by a square) are modelled with single beam elements, while the horizontal ones (marked with triangles) are divided by two beam elements (Fig. 4d). All diagonal struts are discretised by two to eight beam elements and comparisons are made to determine the optimum mesh size. Fig. 4c and b present the two cases where 8 and 4 beam elements are used to

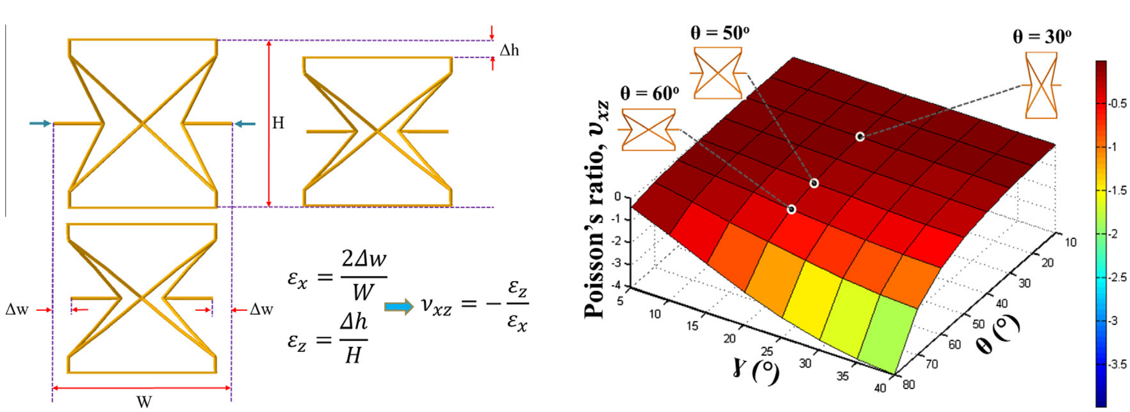

Fig. 3. Calculation procedure for effective Poisson's ratio $\boldsymbol{\nu_{xz}}$ of the auxetic unit cell (left) and dependence of $\boldsymbol{\nu_{xz}}$ on geometrical parameters of the unit cell (right).

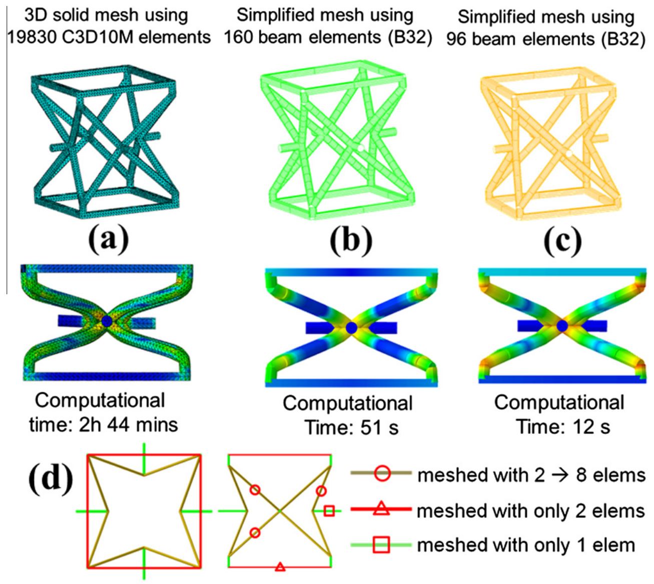

Fig. 4. Two approaches for modelling the auxetic unit cell structures including a full 3D tetrahedral mesh (a) and beam-based models (b and c). All the diagonal struts (representatively marked by red circles) in the beam models are discretised by 2 to 8 elements (d), while the rest is modelled by 1 or 2 elements (representatively marked by triangle and square labels). All diagonal beams in (c) are discretised with 8 elements and 4 elements in the (b) case. (For interpretation of the references to colour in this figure legend, the reader is referred to the web version of this article.)

describe the diagonal struts, respectively. Beam mesh sizes are kept unchanged for the horizontal and vertical truss members in this study.

Both models are subjected to compression at a high strain rate of 500 s^{-1} until reaching a total strain value in the vertical direction of 0.66. Vertical displacements are imposed on the upper facets of the unit cell with the simply supported bases. A "*hard*" contact option is chosen for the normal contact behaviour of the AU, while the friction coefficient for the tangential contact is set at 0.5 with a penalty formulation. The deformation and stress contour of each model is presented in Fig. 4, demonstrating similar auxetic behaviours. The eight-beam model seems to capture the curvatures of the bent struts better, when compared with the solid model. Reaction forces and absorbed energy are used to evaluate and compare the solid and beam models.

Comparisons between different AU models and the convergence study on the mesh size of the beam models are presented in Fig. 5 in terms of plastic dissipated energy and reaction forces measured at the base of the AUs. In cases where the number of beam elements is larger than two in diagonal struts, beam-based models capture the behaviours of the full 3D one very well. In other words, Fig. 5 shows that four beam elements for the diagonal struts are sufficient to effectively simulate the AU structure under dynamic compression. For other cases with more beam elements in the diagonal struts, there are slight differences near the end of the compact phase of the AU, which could relate to the fact that ABAQUS automatically reduces the radius of the beam to avoid contact instability problems. The surges of reaction forces at 0.7 ms are caused by the contact of the struts inside the unit cell during the densification process.

It is also noticed in Fig. 4 that the computational time for solving a full 3D solid model is 2 h 44 min, while those for the four-beam and eight-beam cases are 12 s and 51 s, respectively. This simulation time is a significant difference between the two modelling approaches, which have been demonstrated to give similar results (Fig. 5). The calculation time for the 3D solid model would become even more prohibitively expensive for larger-scale assembled structures. As a result, the use of beam elements is reasonable to obtain key dynamic responses of auxetic composite structures.

2.4. Effect of imperfections on the local buckling of auxetic structures

As mentioned earlier, there are various factors during the additive manufacturing process that could affect the mechanical performance of AU struts. Parts fabricated by selective laser sintering (SLS), for example, could be affected by the choices of focus area and energy of laser beams, metal powder sizes, and fabrication speed [41]. These defects are gradually minimised with rapid advancements in additive manufacturing technologies. These defects certainly change the desired topography of the manufactured part, enabling the onset of the buckling under compressive loads. In order to provide comprehensive understanding on the influences of imperfections on the deformations and failure modes of the auxetic structures, summation effect of the imperfections are considered and introduced into the model. These geometrical imperfections are reproduced with a linear superposition of buckling eigenmodes and a proper weight factor for each eigenmode, as follows:

$$\Delta x = \sum_{i=1}^{M} w_i \varphi_i, \quad (2)$$

where φ_i is the ith mode shape and w_i is the associated weight factor. A single unit cell and $5 \times 5 \times 3$ unit cell block for three different AU configurations corresponding to θ values of 30°, 50° and 60° are

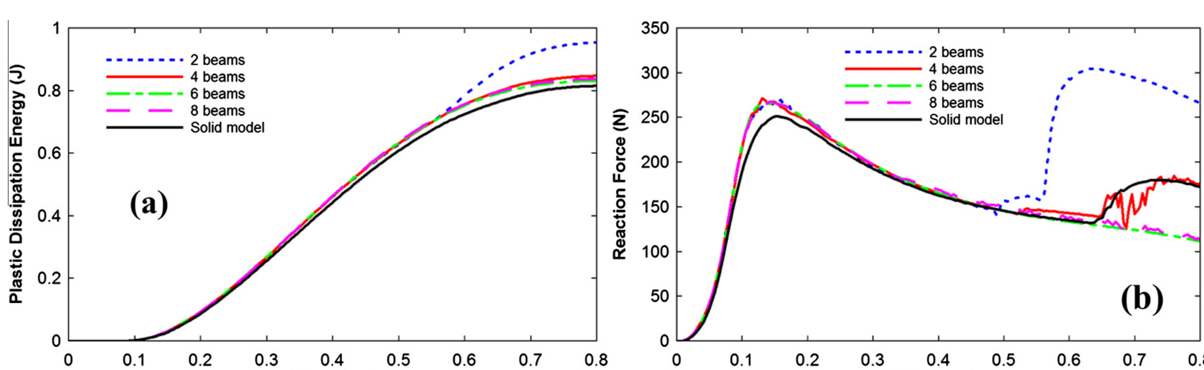

Fig. 5. (a) Time evolutions of plastic dissipated energy, (b) and reaction forces associated with various auxetic unit cell models including the 3D solid and the beam models of different mesh sizes subjected to dynamic compressions. The diagonal struts in the beam models are discretised with different numbers of beam elements (from 2 to 8) for the convergence study.

investigated for buckling effect. The first 50 eigenmodes are extracted from the buckling analyses, and the first 25 of these are added imperfections to their trusses. The associated weight factor is 0.02 mm for the first four modes, which is 5% of the strut diameter; 0.016 mm (4%) for the second group of modes and so on, until the last 10 modes are assigned with only 0.004 mm (1%) weight factor.

In this study, the AUs undergo large deformations ($\varepsilon = 0.66$) when subjected to high strain rate compressions (500 s^{-1}). Deformations for mode 1 to 3 are presented for the baseline model ($\theta = 50°$) and the stress–strain curves are obtained for different configurations associated with different choices of θ. In Fig. 6, the dynamic responses for AUs with integrated buckling imperfections are also presented with the cases without imperfection for comparison. For the cases, where θ is 50° and 60°, the introduced imperfections do not seem to affect the material responses of unit cells as the associated stress–strain curves are coincident. There are, however, some differences for the $\theta = 30°$ case, where the unit cells are taller and more slender. This suggests that the "$\theta = 30°$" unit cell is more likely to buckle due to the stretching-dominated behaviours compared to the other cases, which are bending-dominated when subjected to compression. For energy absorption applications, the bending-dominated unit cells are more favourable as they could transmit a smaller amount of strength for a longer time, and to prevent a softening post-yield response due to buckling of the struts [42]. The presence of defects does not change the behaviour of the structures, but shows an increase of the stretching-dominated behaviour of the $\theta = 30°$ unit cell (Fig. 6).

Fig. 7 presents the effects of imperfections on the buckling modes and material responses of a $5 \times 5 \times 3$ AU block. Mode 1 to 3 deformations are presented for the AU block without imperfections, while the stress–strain curves are plotted to compare between the original and imperfect AU blocks of different Poisson's ratios. Similar to the analysis on the single AU, the AU blocks associated with θ of 50° and 60° exhibit identical structural responses between the original and imperfect models; while differences between the two configurations for the $\theta = 30°$ case are reduced considerably. These investigations suggest that the effects of imperfections in the AU structures will be minimised with the increase in the number of unit cells, and therefore imperfections will not be considered in the following parts of this work.

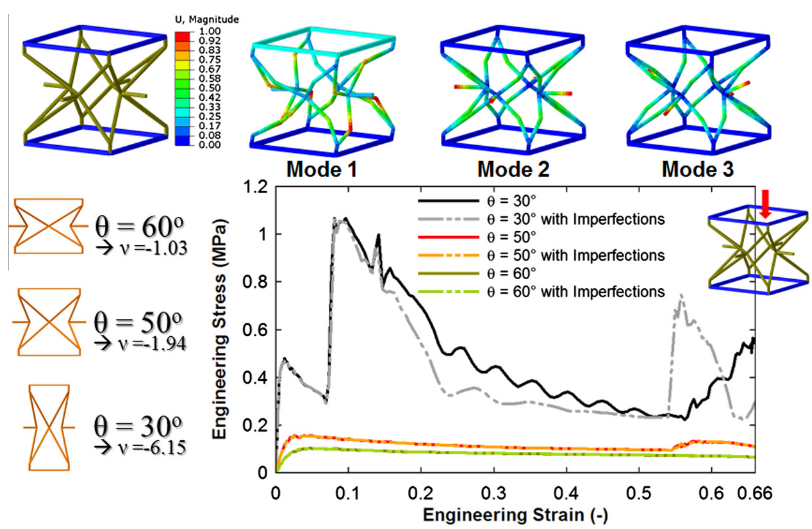

Fig. 6. Influences of imperfections on the deformation modes and the dynamic responses of single auxetic unit cells with different effective Poisson's ratios under large strain (0.66) compression at high strain rates of 500 s^{-1}.

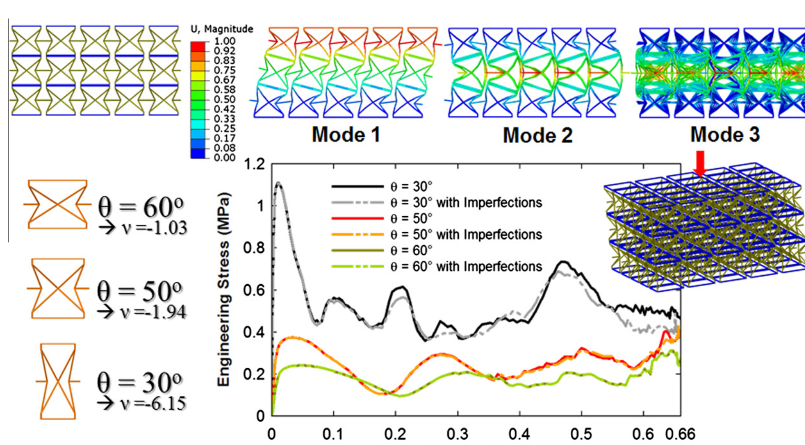

Fig. 7. Influences of imperfections on the deformation modes and the dynamic responses of the $5 \times 5 \times 3$ unit cell block with different effective Poisson's ratios under large strain (0.66) compression at high strain rates of 500 s^{-1}.

2.5. Symmetrical model for auxetic composite sandwich panel

A symmetrical quadrant of the auxetic composite panel (ACP) is modelled to have three layers of auxetic core comprised of $25 \times 25 \times 3$ (1875) auxetic unit cells with a total volume of $300 \times 300 \times 30\ \text{mm}^3$ sandwiched between two metallic facets (presented in Fig. 8). Symmetrical boundary conditions are imposed on the sides delimited by lines OC and OA, while being fixed on the other sides delimited by lines AB and BC. The baseline model, which corresponds to the configuration of $\theta = 50°$, has a 30 mm tall core (each AU is 10 mm tall) and two 2 mm thick facets. The beam radius of the AU strut is 0.2 mm and the entire structure is made from annealed stainless steel (SS304). The rate-dependent material characterisation and properties of metals used for the AU core and sandwich facets are provided in the next section. To effectively design the three-dimensional ACP, three 10 mm tall and 12 mm wide auxetic unit cells are sandwiched between two unit panels, which are modelled by shell elements before being multiplied and assembled into 625 connected units. By this way, all the adjustments in the "seed" AU will be consistently implemented in the entire structure.

In particular, the auxetic core is modelled with 172,500 three-node, second-order Timoshenko beam elements (B32), with 4 beam elements used to discretise the diagonal struts. The metal facets are represented with 22,500 reduced shell elements (S4R) with a mesh size of 2.5 mm. Blast loadings are applied on both the ACP and equivalent monolithic panels with the same areal density and material for comparison. For the baseline case, this monolithic panel is 4.6 mm thick. The solid panel is modelled with 2500 6 mm shell elements (S4R) with reduced integration and hourglass control. Performances of these structures are evaluated in terms of plastic dissipated energy and maximum displacement as well as central velocity evolutions of the back panels.

The numerical investigations to evaluate blast resistant performance of the ACPs are conducted for different configurations that correspond to different values of θ (30–60°), strut radius r (0.2–0.8 mm) and panel thickness t (2–6 mm). Other testing configurations include blast impulses (1–7 MPa ms) and choices of materials (annealed stainless steel 304 [43], AISI 4340 steel [44], and 5083-H116 aluminium alloy). Results from these investigations are compared with equivalent monolithic panels with the same dimensions, areal density and materials. The ACP core is also analysed to evaluate its behaviour at different values of Poisson's ratio, which could result in a bending-dominated structure [45] for lower absolute values of ν, or a stretching-dominated structure [42] at higher absolute values of ν.

2.6. Blast loading description

The ACPs are subjected to blast loads defined by the CONWEP program, which assumes an exponential decay of pressure with time, as follows:

$$P(t) = P_{so}\left[1 - \frac{t - T_a}{T_0}\right] \exp\left[\frac{-A \times (t - T_a)}{T_0}\right], \tag{3}$$

where $P(t)$ is the pressure at time t (MPa); P_{so} is the peak incident pressure (MPa); T_0 is the positive phase duration (ms); A is the decay coefficient; and T_a is the arrival time of the shock wave (ms). The CONWEP airblast model is used to predict of the free-field and reflected airblast parameters due to the detonation of a 150 g spherical charge of TNT explosive at a stand-off distance of 100 mm from the frontal panel of the ACP. The incident and reflected pressure profiles for hemispherical blast waves are predicted by CONWEP and are illustrated in Fig. 9.

Various key outputs from the simulated blast wave could be highlighted here, including the peak pressure of reflected stress wave of 171.7 MPa and the total reflected impulse of 3.6 MPa ms. The arrival time of the stress wave on the structure is 0.018 ms and the duration of the positive phase is 0.1 ms. The corresponding decay coefficient is calculated to be 0.029.

3. Material characterisation and models

In this study, different materials have been used for the external facets and the auxetic core of the auxetic sandwich panel. The

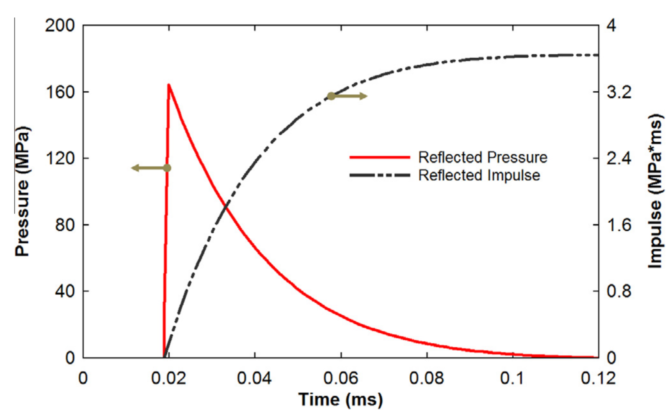

Fig. 9. Time histories of reflected pressures and impulses applied on the auxetic composite structure.

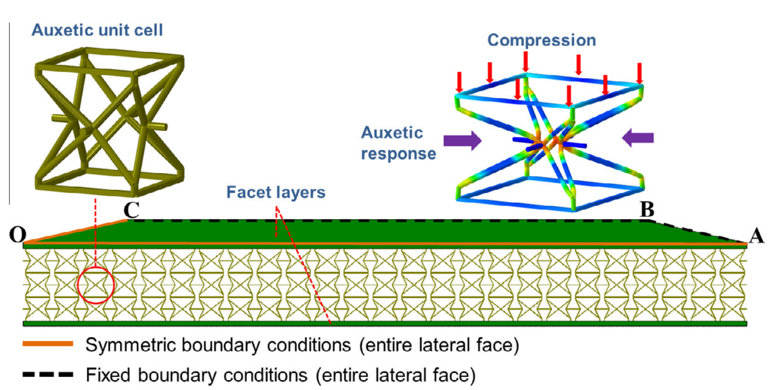

Fig. 8. Schematic design of auxetic composite sandwich panel. Only a quadrant of the panel is modelled due to symmetry of the structure and loading. The symmetrical boundary is denoted by OC and OA, while the panel sides aligned with edges BC and BA are fixed.

material properties of the ACP's components under high-speed impact or blast loadings are expected to be rate-dependent and, therefore, low-to-high strain rate material characterisations are required to obtain accurate constitutive models. There are only few studies conducted in literature to obtain the quasi-static material properties [34,1] for 3D auxetic structures subjected to impulsive loadings. For the baseline structure, the rate-dependent properties of annealed SS304 steel are adopted from previous works [35]. This particular steel has a reduced yield strength and higher ductility when compared with others due to the annealing manufacturing process. The other option for steel is AISI 4340, which was developed in previous work [36], and could be utilised for both the auxetic core and monolithic plates. This steel is commonly used for ballistic purposes [37], which offers higher yield strength and lower ductility.

Aluminium alloy 5083-H116 has been also employed for the auxetic core for its high energy absorption-to-weight ratio. This aluminium alloy has been used considerably in soft armour and protective structures industries due to its low density, high ductility and anti-corrosive properties in comparison with steel alloys. With the aim of utilising this aluminium alloy as one of the material components of the composite bollard, dynamic tests are performed to obtain the rate-dependent properties of aluminium 5083-H116. Two different test setups are used, including the Split Hopkinson Pressure Bar (SHPB) method for high strain rate tests and the Instron tensile testing machine for medium-to-low strain rate tests. Stress–strain behaviour was obtained for the material under strain rates in the range of 10^{-3}/s–10^{4}/s. Besides the majority of aluminium content, the alloy AA 5083-H116 (AA5083) has other chemical compositions, as indicated in Table 1.

The alloy AA5083 belongs to the aluminium 5000 series fabricated with magnesium as the major component. The tensile tests are performed using the Instron VHS 8800 system, with a maximum stretching velocity of 25 m/s. The SHPB is used for the medium-to-high strain rate tests. The specimen is sandwiched between two pressure bars and loaded by a single travelling pulse, either in compression or tension. The pulse signals are monitored with the aid of strain gauge transducers, where simultaneous recordings can be obtained for stress versus time and strain rate versus time. By varying the impact velocity in the SHPB test, strain rates up to 10^{4}/s can be obtained.

In order to develop the material model to capture the rate-dependent behaviour of this aluminium alloy, the Johnson–Cook strength model [46], which is a phenomenological model based on various experiments, has been employed. In its simplest form, only five parameters have to be determined by means of material tests. The original Johnson–Cook model is defined as:

$$\sigma_{eq} = \left[A + B\varepsilon_{eq}^{n}\right][1 + C\ln\dot{\varepsilon}^{*}][1 - T^{*m}], \tag{4}$$

where σ_{eq}, ε_{eq}, $\dot{\varepsilon}^{*}$ denote the von Mises equivalent flow stress, equivalent plastic strain, and dimensionless plastic strain rate, respectively. The term $\dot{\varepsilon}^{*}$ is defined by the ratio $(\dot{\varepsilon}/\dot{\varepsilon}_0)$, in which $\dot{\varepsilon}_0$ is the reference strain rate, which is set to 10^{-3}/s for this model. The dimensionless temperature T^{*} is defined by the ratio $(T–T_r)/(T_m–T_r)$, where T is the material temperature, T_r is the room temperature and T_m is the melting temperature. In Eq. (4), parameter A is the plastic yield stress, B and n are two parameters controlling the development of strain hardening, and the second bracketed term concerns the strain rate hardening. Parameters A, B, C and n are derived from the experimental results, while the temperature parameters T_m and m are obtained from [47] for a similar material. The experiment is conducted at room temperature (T_r = 20 °C). Overall material properties of the three chosen materials are presented in Table 2.

4. Numerical results

4.1. Blast resistance performance of the baseline auxetic composite panel

The baseline model for an auxetic composite panel (ACP) is firstly analysed in this work. The ACP is composed of the metallic auxetic core and two facets, with its key design parameters including shape factors θ = 50°; γ = 20°; L = 6.7 mm; beam radius r = 0.2 mm; and composite facet t = 2 mm. The relative density of the auxetic core is computed by Eq. (1) as 1.95%. The applied blast loading of 150 g TNT is equivalent to an impulse of 3.643 MPa ms. The deformation of the ACP under blast impulse is presented in Fig. 10, showing the cross-section view at 0.18 ms after impact. The frontal panel is deformed plastically, crushing the auxetic core before, without affecting the back panel. The von Mises stress level is set at 700 MPa, which exceeds the yield strength of the annealed steel SS304 used for both the core and facets in the baseline model. Due to the spherical blast wave created by the CONWEP model, stresses are more concentrated at the centre of the panel, and progressively spread to the entire panel along with the imparted shockwave. The close-up view of the ACP panel at 0.36 ms reveals the further deformation of the frontal facet and auxetic core, leading to deflection of the back plate. The crushing regions of the panel at 0.36 ms are observed to be trailing further away from the centre due to the transient effect.

After the initial stress concentration at the centre of the panel, the effect of the auxetic core has helped distribute the concentrated load to a larger region, as seen in the later stage. The roles of the composite facets are evident in facilitating the transfer of blast impulse and in protecting the core from localised damages. Fig. 11 presents the comparison of blast resistance performance of the ACP and an equivalent monolithic panel of similar materials and areal mass. In particular, Fig. 11a displays the time evolutions of displacements (left axis) and total plastic dissipated energy

Table 2
Material properties and Johnson–Cook parameters of annealed SS304 [43], AISI 4340 steel [44], and AA5083-H116.

	Annealed SS304	AISI 4340 steel	AA5083-H116
ρ (kg/m^3)	7900	7850	2750
E (GPa)	200	210	70
v	0.3	0.3	0.3
T_M (K)	1673	1800	893
T_r (K)	293	293	293
A (MPa)	310	792	215
B (MPa)	1000	510	280
n	0.65	0.260	0.404
C	0.07	0.014	0.0085
$\dot{\varepsilon}_0$ (s^{-1})	1.00	5×10^{-4}	1×10^{-3}
m	1.00	1.03	0.859

Table 1
Chemical composition of the tested aluminium alloys. The alloy constituent materials are indicated as percentage of total weight.

Materials	Si	Fe	Cu	Mn	Mg	Cr	Zn	Ti	Others
AA5083-H116	0.4	0.4	0.1	0.4–1.0	4.0–4.9	0.05–0.25	0.25	0.15	0.15

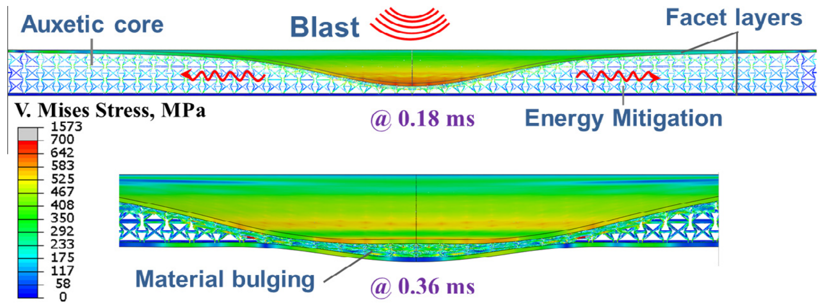

Fig. 10. Blast loading on the "standard" auxetic sandwich panel. The bulging of the panel is evident at 0.36 ms after the blast load. This behaviour determines the deflection of the blast wave and its mitigation.

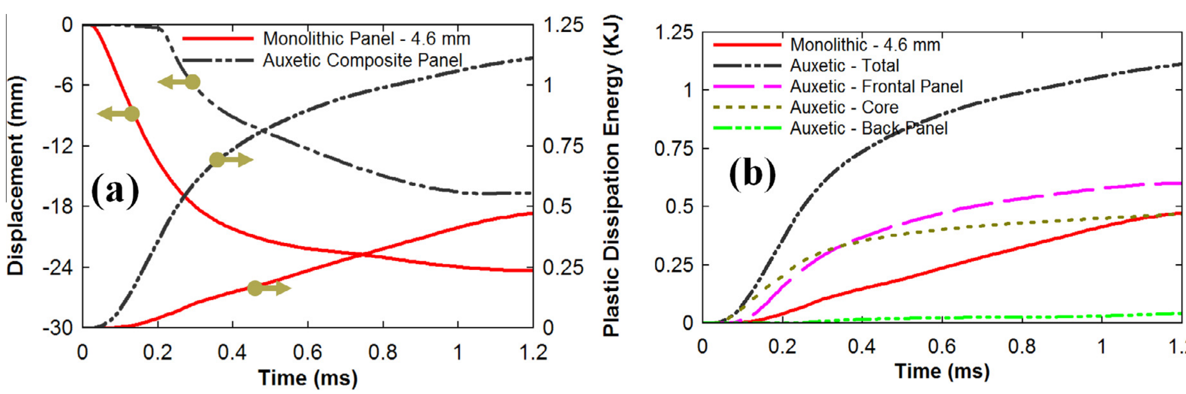

Fig. 11. Comparisons of maximum back facet displacements and plastic dissipated energies (a) for the auxetic sandwich panel and the equivalent monolithic panel of similar material and areal mass under blast loading; individual plastic dissipation components associated with the facets and the auxetic core are also presented in (b).

(right axis) of the two investigated panels. The equivalent monolithic panel has a thickness of 4.6 mm.

As clearly seen in Fig. 11a, the ACP with an auxetic core has significantly reduced the maximum back-facet displacement at 1.2 ms from 24 mm for the monolithic panel to 17 mm for the ACP. There is also about 0.2 ms delay in the back-facet deformation of the ACP compared with that of the monolithic one due to the crushing effect of the auxetic core. The total plastic energy dissipation presented in Fig. 11a also demonstrates the influence of the auxetic core on the energy absorption capacity of the ACP. In particular, the ACP dissipated plastic energy twice as much as the monolithic one. Further analysis on the plastic energy dissipations of the ACP's individual components, including the front and back facets as well as the auxetic core, is presented in Fig. 11b. The majority of energy is absorbed by the frontal plate and the auxetic core, while there is only a small amount of energy dissipated through bending of the back facet.

4.2. Blast performance comparisons for different shapes of the auxetic unit cell

As described earlier, by changing the geometrical parameter θ, different auxetic unit cells could be obtained, which vary in the value of effective Poison's ratio. By assembling these unit cells into the ACP, different composite panels are achieved with different heights and relative densities. In this work, three representative ACPs associated with three values of θ (30°, 50° and 60°) are subjected to similar blast loading and evaluated. In order to obtain the same areal density for different unit cells, the radii of the struts are varied. A summary of various design parameters for the three representative unit cell models are presented in Table 3.

All the panels are subjected to similar blast loading, and the von Mises stress distributions of the deformed panels (including the monolithic one) are illustrated through the cross-section views in Fig. 12. Due to the difference in the design parameter θ, the height of these panels are increased from $\theta = 60^o$ to $\theta = 30^o$. This difference is associated with the delay in deformation of the back panels due to longer compression times for auxetic cores.

The top views of the ACPs and the corresponding monolithic panel are presented in Fig. 13 as snapshots of the von Mises stress contours. As clearly seen from this figure, the stress patterns are quite different for each panel depending on the interactions between the frontal facets and auxetic cores with the back layer. The ACPs evidently show better stress distributions across panels compared with more concentrated force in the monolithic one. The square reflected wave rings on these panels could be associated with the boundary effect of the panels, while the circular ones are related to the stress waves generated from the centres of the panels.

Table 3
Design parameters for the three unit cell models.

θ	ν	r (mm)	Relative density ρ^* (%)	Areal density (kg/m^2)	Equivalent panel thickness (mm)
30°	−6.15	0.18	1.97	36.34	4.60
50°	−1.94	0.2	1.96	"	"
60°	−1.03	0.19	1.97	"	"

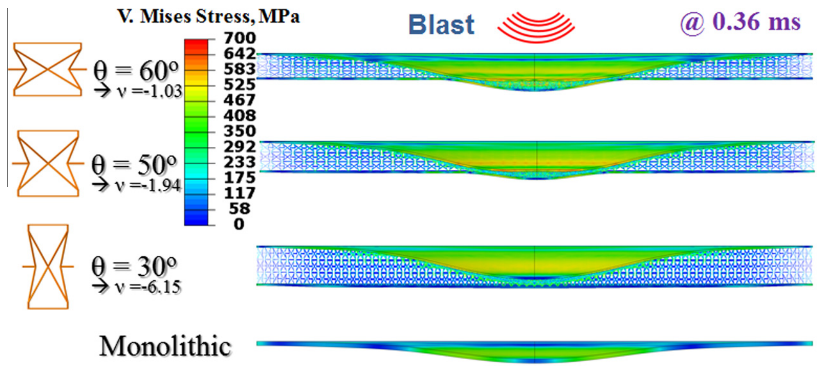

Fig. 12. Cross-section snapshots at 0.36 ms of the deformed auxetic composite and monolithic panels constructed from different auxetic unit cell designs. All panels have similar areal mass density and vary in height due to the shape factor.

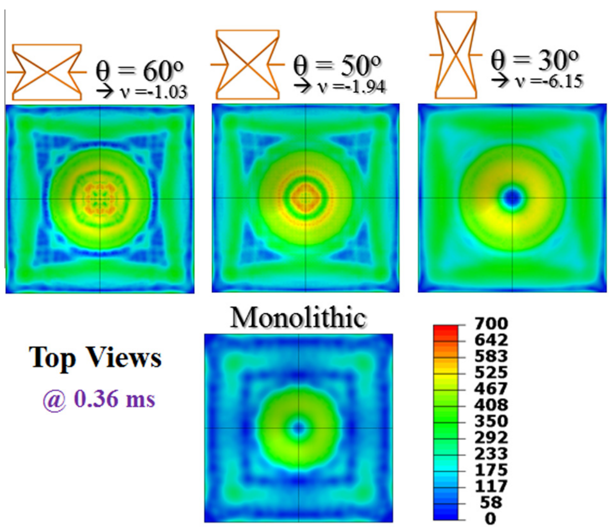

Fig. 13. von Mises stress distributions on the frontal facet of the four panels at 0.36 ms.

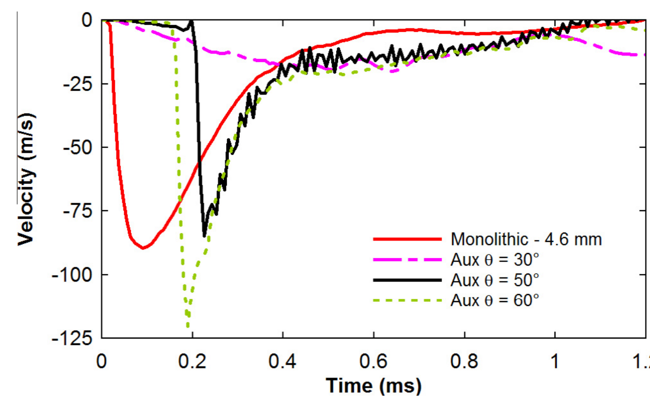

Fig. 15. Comparisons of back facet centre velocities for the auxetic sandwich panels and the equivalent monolithic panel under blast loading.

Comparisons between central deflections and plastic dissipated energy of the four panels are presented in Fig. 14. Evidently, the ACP structures help to reduce the maximum displacement of the back facet up to 45% when compared with the monolithic one. For $\theta = 60°$, the corresponding ACP has a similar deflection at 1.2 ms compared with the monolithic panel. The difference in displacement prior to 1.2 ms is due to the time to compress the cores. The ACP composed of $\theta = 60°$ unit cells, which have the smallest thickness, do not seem to have much advantage compared to the monolithic panel. Moreover, for $\theta = 50°$ and 30°, there is considerable improvement in displacements. The ACP associated with $\theta = 30°$ is the thickest, offering the best back facet displacement reduction. However, this particular ACP could have some limitations due to the higher chance for buckling and restricted thickness of the panel. Fig. 14b shows comparisons of plastic dissipated energy, which indicate negligible differences in energy absorbed through plastic deformation among the ACPs. It is also clearly shown that all the ACPs dissipate significantly more energy compared with the monolithic one.

Fig. 15 presents comparisons of time evolutions of central out-of-plane velocities for three ACPs and a monolithic panel. The maximum back facet velocities achieved by the three ACPs ($\theta = 30°$, 50° and 60°) are 20, 84 and 120 m/s, respectively, compared with 89 m/s of the monolithic panel. As clearly shown in Fig. 15, the ACP associated with $\theta = 30°$ induces the back facet deformation

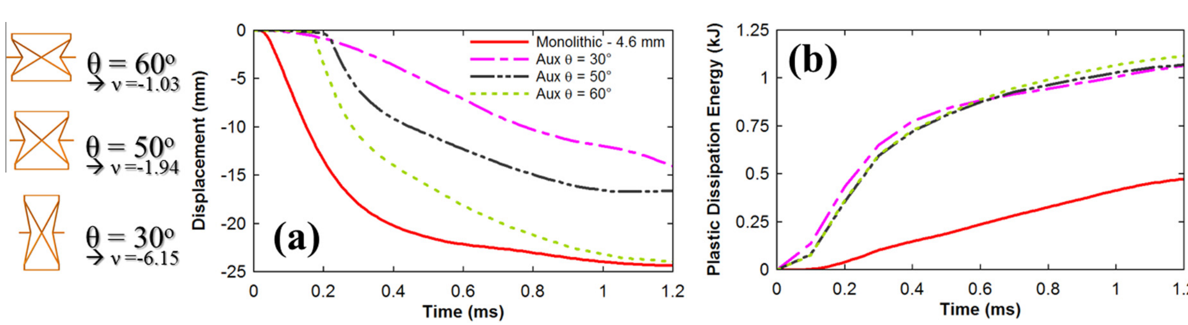

Fig. 14. (a) Comparisons of maximum back facet displacements, and (b) plastic dissipated energies, for three auxetic sandwich panels and an equivalent monolithic one under blast loadings.

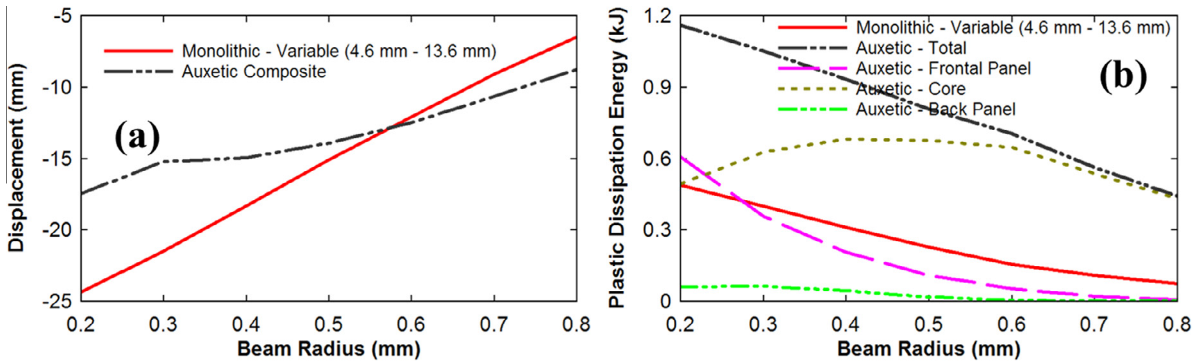

Fig. 16. Comparisons of (a) maximum back facet displacements, and (b) plastic dissipated energies, for the auxetic sandwich panel and an equivalent monolithic panel under blast loading for different strut radii from 0.2 to 0.8 mm.

rate, while the ACP associated with $\theta = 60°$ gives a sharp jump in velocity exceeding that of the monolithic one. At the end of the core compression-induced densification process, the $\theta = 60°$ auxetic composite panel behaves like a solid one, which increases the local stiffness and density.

It should be noted that imperfections are not added to the above ACP models. Earlier studies on the influences of imperfections indicated that this factor is insignificant for auxetic unit cells associated with $\theta = 60°$ and $\theta = 50°$. There is, however, possibility that the performances of the ACP related to $\theta = 30°$ could be affected by the imperfections. However, earlier investigation (Fig. 7) on the behaviours of assembled imperfect unit cells has shown that for a sufficiently large number of unit cells in the assembly, the effect of imperfection is considerably minimised.

5. Parametric studies and discussions

5.1. Influences of strut thickness

The blast resistance performances of the ACPs are dependent on the slenderness of strut elements in the auxetic unit cells. Fig. 16 presents an investigation of the influences of strut radius on the deformation and dissipated energy evolutions of the ACPs under blast loadings. As the areal densities of ACPs vary with strut thickness, the equivalent monolithic panels have thicknesses ranging from 4.6 to 13.6 mm. Further details on the key parameters of auxetic unit cells and the ACPs, including relative density and areal mass density, are summarised in Table 4. Other design parameters of the unit cells are similar to those of the baseline case except the radius value.

It can be seen from Fig. 16 that the ACPs with smaller radii tend to perform better in both central deflection and plastic energy dissipation compared to thicker strut cases. There is a transition point at $r \approx 0.55$ mm (Fig. 16a), where the monolithic panel deflects less than the equivalent ACP, which could be attributed to the enhanced stiffness of the auxetic cores. On the other hand, for any radius value, the ACPs always absorbed more imparted energy than the equivalent monolithic panel. Fig. 16b also presents the breakdown contributions to plastic deformation energy of individual ACP components. As mentioned earlier, the manufacturing of auxetic unit cells of certain strut radii is dependent on the additive manufacturing technologies which are constrained in both resolution and minimum wall thickness of about 0.2 mm.

Table 4
Properties of the numerical models for different radii.

r (mm)	Relative density ρ^* (%)	Areal density (kg/m^2)	Eq. panel thickness (mm)
0.2	1.96	36.34	4.6
0.3	4.41	42.27	5.4
0.4	7.84	50.56	6.4
0.5	12.25	61.23	7.8
0.6	17.64	74.26	9.4
0.7	24.00	89.67	11.4
0.8	31.35	107.44	13.6

5.2. Influences of composite panel frontal facet

The composite facets, as mentioned earlier, are critically important, especially the frontal plate, to protect the core from localised damages due to impulsive loadings and to maximise the energy absorption by distributing blast loads to the entire ACP structure. By increasing the thickness of the panel, the stiffness is clearly enhanced along with the higher areal mass of the ACP, which needs to be optimised (see Table 5).

As can be seen from Fig. 17a, the gap between the maximum deflections of the ACPs and the corresponding monolithic panel is decreased as the thickness of the frontal facet increases. Using thicker facets leads to a stiffer ACP structure with higher areal density and reduces the role of the auxetic core. Similar conclusions could be seen from Fig. 17b, showing the plastic dissipated energy for the ACP, monolithic panel and individual components. The energy absorbed by the core through plastic deformation decreases along with the increase of the facet's thickness, and the performances of the ACPs asymptotically approach the monolithic ones.

5.3. Effects of blast impulse

By varying the amount of TNT explosives, different blast impulses are achieved and are summarised in Table 6. The rate-dependency effects of the ACP materials are expected to generate nonlinear dynamic responses of composite panels against different blast loads.

Fig. 18a presents the dependence of the ACP's back facet central displacement and the corresponding monolithic one on the magnitude of blast impulse. For the monolithic one, the maximum

Table 5
Properties of the numerical models for different frontal panel thicknesses.

t (mm)	Relative density, ρ^* (%)	Areal density (kg/m^2)	Eq. panel thickness (mm)
2	1.96	36.34	4.6
3	"	44.24	5.6
4	"	52.14	6.6
5	"	60.04	7.6
6	"	67.94	8.6

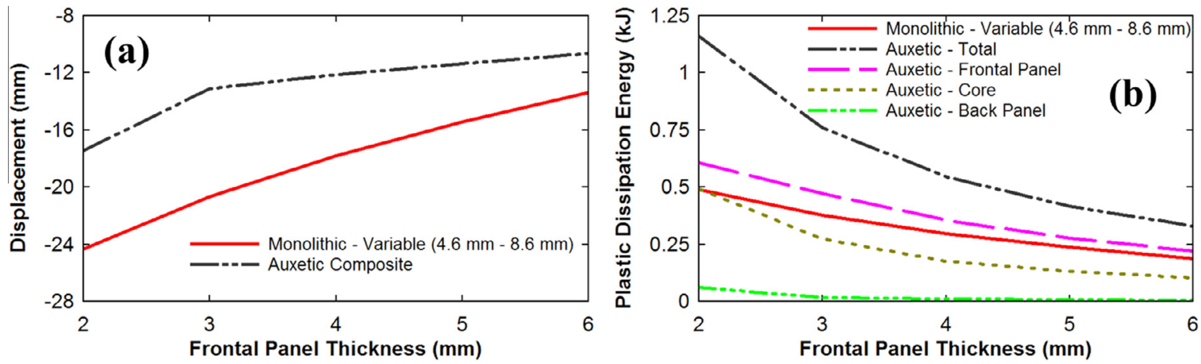

Fig. 17. Comparisons of (a) maximum back facet displacements, and (b) plastic dissipated energies, for the auxetic sandwich panels and an equivalent monolithic panel under blast loading for different facet thicknesses from 2 to 6 mm.

Table 6
Characteristics of different blast loadings.

TNT (g)	Stand-off distance (mm)	Reflected overpressure (MPa)	Impulse (MPa ms)
50	100	98.7	1.37
100	"	141.5	2.53
150	"	171.7	3.64
200	"	195.8	4.74
300	"	233.4	6.90

displacement varies linearly with the impulse, while that of the ACP exhibits a nonlinear relationship. According to this analysis, when the impulse is below 4.8 MPa ms, the ACP performs better than the monolithic one in terms of maximum deflection. Higher values of impulse seem to compress the core quickly, leading to a rapid local densification at the centre of the panel and therefore inducing a higher deflection rate and displacement.

Fig. 18b compares the dependencies of maximum dissipated energy through the plasticity of various components of the ACP and the monolithic panel. As clearly seen in this figure, the total energy dissipated in the ACP is always double that of the solid one for different impulses. The frontal panels dissipate as much energy as the auxetic core, while the back facets absorb the least. As the impulse energy exceeds the threshold of 4.8 MPa ms, the cores could not behave effectively, as discussed earlier, leading to the sudden increase in the plastic dissipated energy of the back metal plates.

5.4. Influences of material choices

Different choices of materials for the auxetic cores and metal facets could have a remarkable impact on the performance of the structure under impulsive loads. So far, the annealed SS304 [43] has been employed in all the above analysis for both the auxetic cores and the facet panels. In this section, the aluminium alloy AA5083-H116 and AISI 4340 steel [44], which were described earlier in Section 3, are considered as alternative options to enhance the stiffness and energy absorption. The following analyses are designed and conducted on composite structures of similar areal density and a summary of the design metrics are presented in Table 7. Equivalent panels made with annealed SS304 and AISI 4340 steel to have similar areal mass are compared with the corresponding ACPs. The beam radii and frontal panel thickness of the ACPs are also changed accordingly to have a similar areal density. The rate-dependent properties of the above materials were summarised previously in Table 2.

AISI 4340 and AA5083-H116 alloy are armour-graded materials, which have higher stiffness and energy absorption capability, respectively, compared with the annealed SS304. A monolithic panel with equivalent areal density made of AISI 4340 is numerically evaluated to compare with the associated ACPs. The baseline case is indicated by the "*" in Table 7.

Similar to previous comparison studies, the maximum displacements at the centre of the back facets are reported in Fig. 19a for different choices of material systems. Under blast loadings, the monolithic panel made of AISI 4340 reduces the back facet maximum deflection significantly lower than that of the baseline ACP (with the auxetic core and facets made of SS304), while dissipating much less energy through plastic deformation (Fig. 19b). The composite sandwich panel with the SS304 auxetic core and AISI 4340 facets reduces the back facet displacement by more than 50% when compared to the baseline case. The use of facet panels with aluminium alloy AA5083-H116 with high yield strength also helped

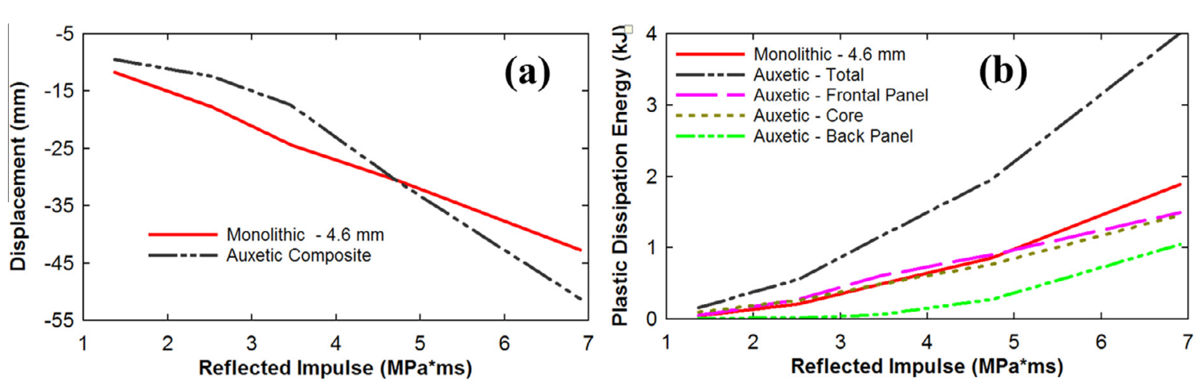

Fig. 18. Comparisons of (a) maximum back facet displacements, and (b) plastic dissipated energies, for the auxetic sandwich panel and an equivalent monolithic one under different blast impulses from 1 to 7 MPa ms.

Table 7
Design metrics for different materials.

Core mat.	Facet mat.	r (mm)	t (mm)	ρ^* (%)	Areal density (kg/m^2)	Eq. panel (mm)
Ann. SS304	AISI 4340	0.20	2.00	1.96	36.34	4.60
Ann. SS304	AA5083-H116	0.20	5.75	“	“	“
*Ann. SS304	*Ann. SS304	0.20	2.00	“	“	“
AISI 4340	AISI 4340	0.20	2.00	“	“	“
AA5083-H116†	AISI 4340†	0.34	2.00	5.63	“	“
AA5083-H116	AISI 4340	0.20	2.00	1.96	33.25	4.21

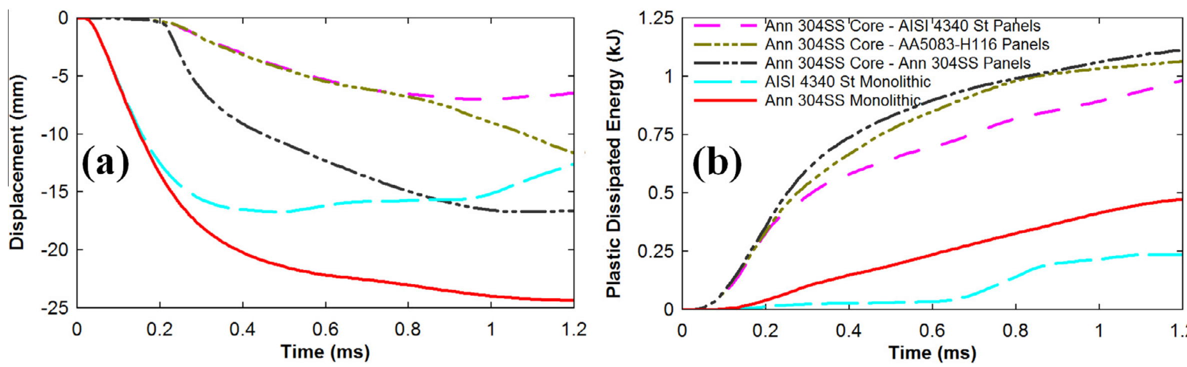

Fig. 19. Comparisons of (a) maximum back facet displacements, and (b) plastic dissipated energies, for the auxetic sandwich panel and the equivalent monolithic one under blast loading for different panel materials.

to significantly reduce the maximum displacement and maximise plastic dissipation. Maximum back facet velocities are also reported in Table 8 for all ACP configurations and corresponding monolithic panels. Compared to the results obtained from the baseline model (*) and equivalent panels made of SS304 and AISI 4340, the other auxetic sandwich panels reduce the maximum rear plate's velocity considerably, up to 80%. The use of aluminium alloy cores seems to reduce the back facet's maximum velocity the most.

Table 8
Comparisons of maximum back facet central velocities (m/s) of ACPs and those of equivalent monolithic panels.

Core	Facets	ACPs	SS304 eq. panel	AISI 4340 eq. panel
Ann. SS304	AISI 4340	21.47	89.48	86.89
Ann. SS304	AA5083-H116	32.88	“	“
*Ann. SS304	*Ann. SS304	84.75	“	“
AISI 4340	AISI 4340	25.27	“	“
AA5083-H116†	AISI 4340†	23.26	“	“
AA5083-H116	AISI 4340	16.26	99.05	96.05

The effects of the core material are also investigated by comparing the four cases (in rows 1 and 4–6, Table 8) of different core materials while using the same AISI 4340 steel facets. In the first three models, the auxetic cores have a similar beam radius made of different materials (AISI 4340, SS304 & AA5083-H116), while the fourth case (indicated by †) has a larger beam radius to achieve a similar areal density. As shown in Fig. 20, the choice of core material affects the deflections and plastic dissipated energy of the ACPs. The back facet's maximum displacement seems to have the smallest value for the AISI 4340 steel core (Fig. 20a), and the largest dissipated energy (Fig. 20b). It is also interesting to note that the AA5083-H116 core with smaller strut radius, which reduces its areal density, performs better. This observation indicates the importance of geometric factor on the effectiveness of the auxetic core in absorbing impulsive loadings. Furthermore, the maximum back facet velocity of the AA5083-H116 core with smaller beams is 16.26 m/s (Table 8), which is smaller than the case with bigger struts. This reduction of velocity could be attributed to a faster plastic deformation of the core under the compressive load.

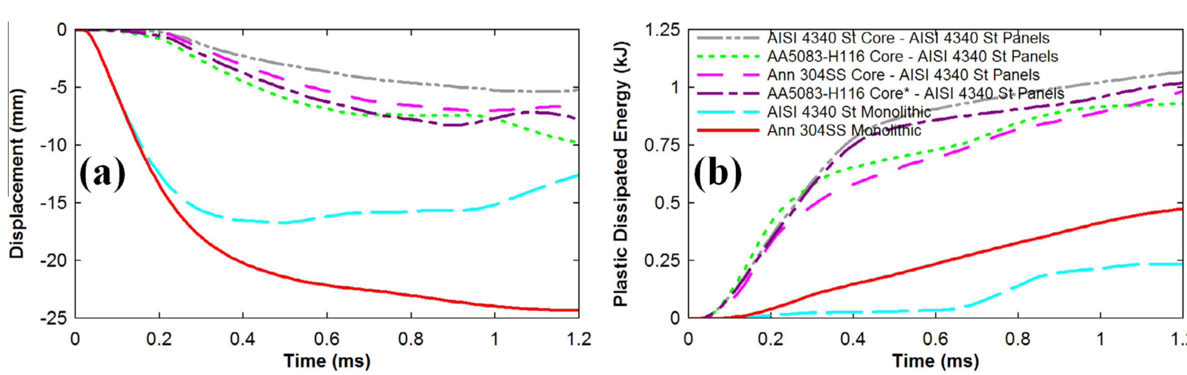

Fig. 20. Comparisons of (a) maximum back facet displacements, and (b) plastic dissipated energies, for the auxetic sandwich panels and equivalent monolithic ones under blast loadings for different auxetic core materials.

6. Conclusions

Numerical investigations of the dynamic responses and energy absorbing capabilities of auxetic composite panels and equivalent monolithic steel plates were conducted. The composite sandwich panels were designed by assembling multiple layers of identical auxetic unit cells and two front and back facets. The Poisson's ratio and auxetic behaviours of the auxetic composite panels (ACPs) were controlled by changing the geometrical parameters and dimensions of the unit cells and thicknesses of the facets. The auxetic unit cells were modelled with beam elements to reduce computational cost, while convergence studies and buckling analyses were performed to ensure reliability of the simplified model. The baseline and parametric analyses were conducted using annealed steel SS304 for both composite facets and the auxetic core to investigate the influences of design parameters and blast loadings. Considerable performance improvements in terms of back facet displacement, velocity and energy absorption were obtained for the ACPs when compared with equivalent monolithic panels. In particular, 30% reduction in back facet displacement and 50% increase in plastic energy dissipation was achieved by the ACPs under blast loadings. Time evolutions of various dissipated energy components associated with the facets and core were presented to highlight the important roles of the frontal facet and auxetic core. Although parametric analyses on the effect of effective Poisson's ratio (PR) indicated an enhancement in structural performance against impulsive loadings for lower effective PR, there are limitations associated with the buckling and desired thickness of the ACPs. Analysis of the beam thickness demonstrated that an increase of strut radius could enhance the core's stiffness, thus reducing the auxetic effects and energy absorption capabilities. Although slender beams could provide better energy absorption performance, current additive prototyping technology has limitations in manufacturing beams of less than 0.2 mm in radius. Other parametric studies on facet thickness and blast loadings showed the sensitiveness of frontal panels and cores to loading conditions, which could be optimised for particular impulses. Different choices of materials were chosen for the facets and the core of the ACP models, and were compared against similar blast loading. The choices of materials for the auxetic core seemed to be less influential compared with those for the facets. The role of the frontal facet is to provide protection for the auxetic core from direct contact with the blast wave and to effectively distribute the impulsive load and, therefore, no fractures or damage models are considered in this work. The proposed auxetic composite sandwich panels are promising structures for protective applications against blast loadings. Further numerical design and future experiments are prepared to validate the concept.

Acknowledgements

This research was sponsored by the Commonwealth Scientific and Industrial Research Organisation (CSIRO) and was accomplished through the Future Manufacturing Flagship program (Dr. Swee Mak, Program Director).

References

[1] Qi C, Yang S, Yang L-J, Wei Z-Y, Lu Z-H. Blast resistance and multi-objective optimization of aluminum foam-cored sandwich panels. Compos Struct 2013;105:45–57.
[2] Flores-Johnson EA, Shen L, Guiamatsia I, Nguyen GD. A numerical study of bioinspired nacre-like composite plates under blast loading. Compos Struct 2015;126:329–36.
[3] Tran P, Ngo TD, Mendis P. Bio-inspired composite structures subjected to underwater impulsive loading. Comput Mater Sci 2014;82:134–9.
[4] Wei X, Tran P, de Vaucorbeil A, Ramaswamy RB, Latourte F, Espinosa HD. Three-dimensional numerical modeling of composite panels subjected to underwater blast. J Mech Phys Solids 2013;61(6):1319–36.
[5] Li X, Zhang P, Wang Z, Wu G, Zhao L. Dynamic behavior of aluminum honeycomb sandwich panels under air blast: experiment and numerical analysis. Compos Struct 2014;108:1001–8.
[6] Lakes R. Foam structures with a negative Poisson's ratio. Science 1987;235 (4792):1038–40.
[7] Evans KE, Alderson A. Auxetic materials: functional materials and structures from lateral thinking. Adv Mater 2000;12(9):617.
[8] Bezazi A, Scarpa F. Mechanical behaviour of conventional and negative Poisson's ratio thermoplastic polyurethane foams under compressive cyclic loading. Int J Fatigue 2007;29(5):922–30.
[9] Greaves GN, Greer A, Lakes R, Rouxel T. Poisson's ratio and modern materials. Nat Mater 2011;10(11):823–37.
[10] Assidi M, Ganghoffer J-F. Composites with auxetic inclusions showing both an auxetic behavior and enhancement of their mechanical properties. Compos Struct 2012;94(8):2373–82.
[11] Lakes R, Elms K. Indentability of conventional and negative Poisson's ratio foams. J Compos Mater 1993;27(12):1193–202.
[12] Scarpa F, Pastorino P, Garelli A, Patsias S, Ruzzene M. Auxetic compliant flexible PU foams: static and dynamic properties. Phys Status Solidi (b) 2005;242(3):681–94.
[13] Scarpa F, Yates J, Ciffo L, Patsias S. Dynamic crushing of auxetic open-cell polyurethane foam. Proc Inst Mech Eng C J Mech Eng Sci 2002;216(12):1153–6.
[14] Alderson KL, Simkins VR, Coenen VL, Davies PJ, Alderson A, Evans KE. How to make auxetic fibre reinforced composites. Phys Status Solidi B Basic Solid State Phys 2005;242(3):509–18.
[15] Hou Y, Neville R, Scarpa F, Remillat C, Gu B, Ruzzene M. Graded conventional–auxetic Kirigami sandwich structures: flatwise compression and edgewise loading. Compos B Eng 2014;59:33–42.
[16] Prall D, Lakes R. Properties of a chiral honeycomb with a Poisson's ratio of—1. Int J Mech Sci 1997;39(3):305–14.
[17] Gibson LJ, Ashby MF, Schajer GS, Robertson CI. Mechanics of two-dimensional cellular materials. Proc R Soc Lond Ser A Math Phys Sci 1982;382 (1782):25–42.
[18] Lira C, Innocenti P, Scarpa F. Transverse elastic shear of auxetic multi re-entrant honeycombs. Compos Struct 2009;90(3):314–22.
[19] Grima J, Evans K. Auxetic behavior from rotating squares. J Mater Sci Lett 2000;19(17):1563–5.
[20] Hughes T, Marmier A, Evans K. Auxetic frameworks inspired by cubic crystals. Int J Solids Struct 2010;47(11):1469–76.
[21] Pikhitsa PV, Choi M, Kim HJ, Ahn SH. Auxetic lattice of multipods. Phys Status Solidi (b) 2009;246(9):2098–101.
[22] Bückmann T et al. Tailored 3D mechanical metamaterials made by dip-in direct-laser-writing optical lithography. Adv Mater 2012;24(20):2710–4.
[23] Lee JH, Singer JP, Thomas EL. Micro-/nanostructured mechanical metamaterials. Adv Mater 2012;24(36):4782–810.
[24] Latourte F et al. Design and identification of high performance steel alloys for structures subjected to underwater impulsive loading. Int J Solids Struct 2012;49(13):1573–87.
[25] Maduliat S, Ngo TD, Tran P, Lumantarna R. Performance of hollow steel tube bollards under quasi-static and lateral impact load. Thin Walled Struct 2015;88:41–7.
[26] Tran P, Ngo T, Yang EC, Mendis P, Humphries W. Effects of architecture on ballistic resistance of textile fabrics: numerical study. Int J Damage Mech 2014;23(3):359–76.
[27] Yang C, Tran P, Ngo T, Mendis P, Humphries W. Effect of textile architecture on energy absorption of woven fabrics subjected to ballistic impact. Appl Mech Mater 2014;553:757–62.
[28] Yang EC, Ngo TD, Ruan D, Tran P. Impact resistance and failure analysis of plain woven curtains. Int J Prot Struct 2015;6(1):113.
[29] Nguyen QT, Tran P, Ngo TD, Tran PA, Mendis P. Experimental and computational investigations on fire resistance of GFRP composite for building façade. Compos B Eng 2014;62:218–29.
[30] Nguyen QT, Ngo TD, Tran P, Mendis P, Bhattacharyya D. Influences of clay and manufacturing on fire resistance of organoclay/thermoset nanocomposites. Compos A Appl Sci Manuf 2015;74:26–37.
[31] Wei XD, de Vaucorbeil A, Tran P, Espinosa HD. A new rate-dependent unidirectional composite model – application to panels subjected to underwater blast. J Mech Phys Solids 2013;61(6):1305–18.
[32] Liang Y et al. The response of metallic sandwich panels to water blast. J Appl Mech 2007;74(1):81–99.
[33] Xue Z, Hutchinson JW. A comparative study of impulse-resistant metal sandwich plates. Int J Impact Eng 2004;30(10):1283–305.
[34] Vaziri A, Xue Z, Hutchinson J. Performance and failure of metal sandwich plates subjected to shock loading. J Mech Mater Struct 2007;2(10):1947–63.
[35] Ma Z-D, Bian H, Sun C, Hulbert GM, Bishnoi K, Rostam-Abadi F. Functionally-graded NPR (negative Poisson's ratio) material for a blast-protective deflector. In: NDIA ground vehicle systems engineering and technology symposium. Dearborn, Michigan; 2010.
[36] Schenk M, Guest S, McShane G. Novel stacked folded cores for blast-resistant sandwich beams. Int J Solids Struct 2014;51(25):4196–214.
[37] Evans K, Nkansah M, Hutchinson I. Auxetic foams: modelling negative Poisson's ratios. Acta Metall Mater 1994;42(4):1289–94.

[38] Wicks N, Hutchinson JW. Optimal truss plates. Int J Solids Struct 2001;38(30):5165–83.
[39] Evans A, He M, Deshpande V, Hutchinson J, Jacobsen A, Carter W. Concepts for enhanced energy absorption using hollow micro-lattices. Int J Impact Eng 2010;37(9):947–59.
[40] Dassault Systémes Simulia Corp., P., Rhode Island, USA, Abaqus 6.13-4, User Manual. 2013.
[41] Li P. Constitutive and failure behaviour in selective laser melted stainless steel for microlattice structures. Mater Sci Eng A 2015;622:114–20.
[42] Deshpande V, Ashby M, Fleck N. Foam topology: bending versus stretching dominated architectures. Acta Mater 2001;49(6):1035–40.
[43] Lee S, Barthelat F, Hutchinson J, Espinosa H. Dynamic failure of metallic pyramidal truss core materials – experiments and modeling. Int J Plast 2006;22(11):2118–45.
[44] Adams B. Simulation of ballistic impacts on armored civil vehicles. Master degree thesis at Eindhoven University; 2003.
[45] Gibson LJ, Ashby MF. Cellular solids: structure and properties. Cambridge University Press; 1999.
[46] Johnson GR, Cook WH. A constitutive model and data for metals subjected to large strains, high strain rates and high temperatures. In: Proceedings of the 7th international symposium on ballistics, vol. 21. The Netherlands: The Hague; 1983. p. 541–7.
[47] Clausen AH, Borvik T, Hopperstad OS, Benallal A. Flow and fracture characteristics of aluminium alloy AA5083-H116 as function of strain rate, temperature and triaxiality. Mater Sci Eng A Struct Mater Prop Microstruct Process 2004;364(1–2):260–72.